Three-dimensional constitutive finite element modeling of the Achilles tendon

Giacomo Longo

2015

LUNDS UNIVERSITET
Lunds Tekniska Högskola

Master Thesis

Faculty of Engineering, LTH
Department of Biomedical Engineering
Supervisors: Hanna Isaksson and Hanifeh Khayyeri

Abstract

Tendons connect muscles to bones enabling efficient locomotion. This study focuses on the Achilles tendon, which is the strongest tendon in the body and fundamental for activities like walking, running and jumping. The Achilles tendon is the most frequently subjected tendon when it comes to injuries and ruptures. The best treatment is still debated, because the biomechanics of the tendons is not yet well understood.

Tendons consist of a complex structure of highly organized collagen fibers embedded in a hydrated matrix. Various material models have tried to represent the viscoelastic and highly non-linear behaviour of tendons. By using accurate material models, computer simulations can be used to predict the behaviour of materials under different loading conditions and to provide extensive information about the mechanical response.

This study further develops an existing two-dimensional fiber- reinforced poroviscoelastic model of the Achilles tendon. The model considered that the tendon was a material consisting of collagen fibers, a non fibrillar matrix and fluid flow. All three components were contributing to the total stresses in the tendon. The existing model gave good representations of the stresses, but did not predict physiological direction of the fluid flow. Moreover, for an accurate analysis of the stresses and the fluid flow inside the tendon, the model should be able to be applied to the realistic three-dimensional geometry of the Achilles tendon.

Therefore, this study aimed to modify the existing model to make it suitable for three-dimensional geometries and to substitute the isotropic constitutive model of the fibrillar matrix with an orthotropic constitutive model to predict a physiological direction of the fluid flow. The new model was validated against experimental data from rat Achilles tendons subjected to cyclic tensile loading tests by optimizing the material parameters of the model.

Comparing the developed model with the previous one, the results showed that the three-dimensional finite element formulation generally behaves very similarly to the two-dimensional model. However, it predicts slightly lower hydrostatic pressure, but higher fluid flux. The introduction of an orthotropic matrix influenced the predictions more significantly. The stresses were higher, especially in the matrix, and the prediction of the direction of fluid flow resembled physiological flow. Hence, the flux and the hydrostatic pressure also assumed a physiological behaviour. The ability of the new model to fit the experimental data remained nearly unchanged.

Therefore, the ability of the model to provide information about the mechanics of the Achilles tendon under cyclic loading has been improved. Future work could improve also the mechanics of the fibrillar part and model the interaction between the different components.

Preface

This master thesis project has been conducted by the Department of Biomedical Engineering of Lund University.

I would like to thank, first of all, my supervisors Hanna Isaksson and Hanifeh Khayyeri for the valuable guidance on every aspect of the project. I would like to thank also Anna Gustafsson for explaining many details of her work, Lorenzo Grassi for helping solving various problems encountered and all with the rest of the biomechanics group for the nice time spent together.

Giacomo Longo

Contents

1 Introduction

Tendons connect muscles to bones and are responsible for transmitting the force generated by muscular fiber contractions to the bony attachments resulting in locomotion and enhancement of joint stability [1,2]. To accomplish their function, tendons must be able to withstand large forces. This study focuses on the Achilles tendon, which is located in the lower leg connecting the *gastrocnemious* (i.e calf muscle) and the *calcaneous* (i.e heel bone), see Fig.1. The Achilles tendon is the largest and strongest tendon of the human body, as it needs to withstand forces that allow locomotion of the entire body weight (i.e walking, running, jumping) [3].

Injuries of the Achilles tendon result in significant limitations in performing common daily activities and have an even greater impact on sport activities. Workers and athletes that expose their tendons to continuous and prolonged over-demanding forces are at high risk of developing tendinopathies causing pain and reduced functional efficiency, which can ultimately lead to ruptures [2]. Also, an increased incidence of Achilles tendon ruptures has been reported for professional athletes and middle-aged and older people playing sports occasionally [4].

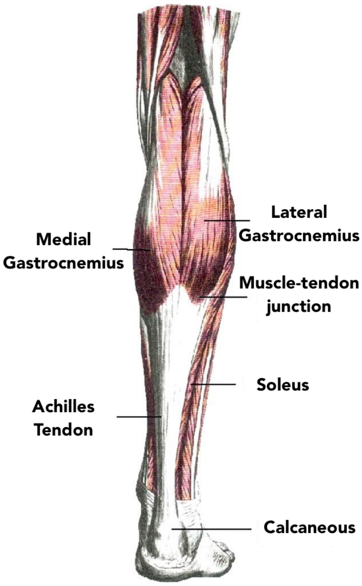

Figure 1: Anatomical posterior view of lower leg [10].

Like other muscoloskeletal tissues, tendons maintain their structural homeostasis by proper external mechanical loading. Mechanical stimuli influence properties of the tendons both in healthy state and during healing [5, 6].

Studies show that active treatments involving controlled loading are able to restore the functionality of the tendon at a higher degree and with shorter rehabilitation times compared to passive healing through immobilization [7–9]. Although, the real efficiency of these clinical routines is not well established, mainly because the biomechanical behaviour of tendons is not yet well understood [2].

To better understand the biomechanics of the tendons and thus to establish proper treatment routines for healing, a precise knowledge of the material behaviour under loading is required. Computational modeling has the ability to simulate the behaviour of a material model under different loading situations and to provide extensive information about the mechanical response.

Various biomechanical models of tendons have been developed. Mainly the tissue has been modeled either at a macroscopic level, as a continuum, or at a microscopic level as a multi-structural material. The latter approach describes the overall behaviour of the tissue as the result of the contribution of different constituents and their mechanical interaction. A better understanding of the mechanical role of the constituents in healthy tendons can be a good starting point for further development aiming to predict failure and later on to model the healing process.

In the biomechanics research group, where this study has been conducted, a 2D non-linear isotropic poroviscoelastic fiber-reinforced model of the Achilles tendon has been previously developed [11] based on an existing model of the cartilage [12, 13]. This is a structural material model of the tissue consisting of a fluid phase and a solid phase divided into a fibrillar and a non-fibrillar part. These represent the three main components of tendons respectively: water, collagen fibers and proteoglycan matrix. Although the model was able to successfully simulate the mechanical behaviour, simplifications were introduced leaving room for further developments. Since the long term aim of the project is to simulate real human Achilles tendon, eventually the model needs to be applied to a real geometry without introducing coarse approximations. Moreover, it was observed that the model simulated inward fluid flow during tension due to the mechanical properties of the non-fibrillar part. Although, experimental studies have shown that tensile loading causes extrusion of water form the inside of the tendon [14], suggesting outward flow. A correct simulation of the direction of the fluid is an essential property of a realistic tendon model. In fact, the fluid behaviour is recognized to be a key factor for the correct modelling of the viscous behaviour of tendons [15, 16].

1.1 Aim of study

The aim of this study is to improve the existing model in two aspects: the geometry and the constitutive model of the non-fibrillar part. First the computational model is developed to simulate cyclic loading on a 3D geometry to allow a more realistic representation of the Achilles tendon geometry. Then the proteoglycan matrix is modeled as an orthotropic hyperelastic material, which is expected to provide mechanical properties capable of simulating a physiological direction of the fluid phase. Both models are validated against experimental data from tensile testing of tendons of rats [17]. Finally, the effects from the developments on the behaviour of the model are evaluated by comparisons with results obtained using the existing 2D axisymmetric tendon model [11].

2 Background

2.1 Tendon composition, structure and function

Tendons are fibrous connective tissue consisting of collagen, elastin, proteoglycans, glycoproteins, cells and water. The dominant cell type are the fibroblasts (tenoblasts and tenocytes), which are responsible for the synthetisation of the extracellular matrix (ECM) proteins, the organization of the collagen matrix and also the remodeling phase of the healing process.

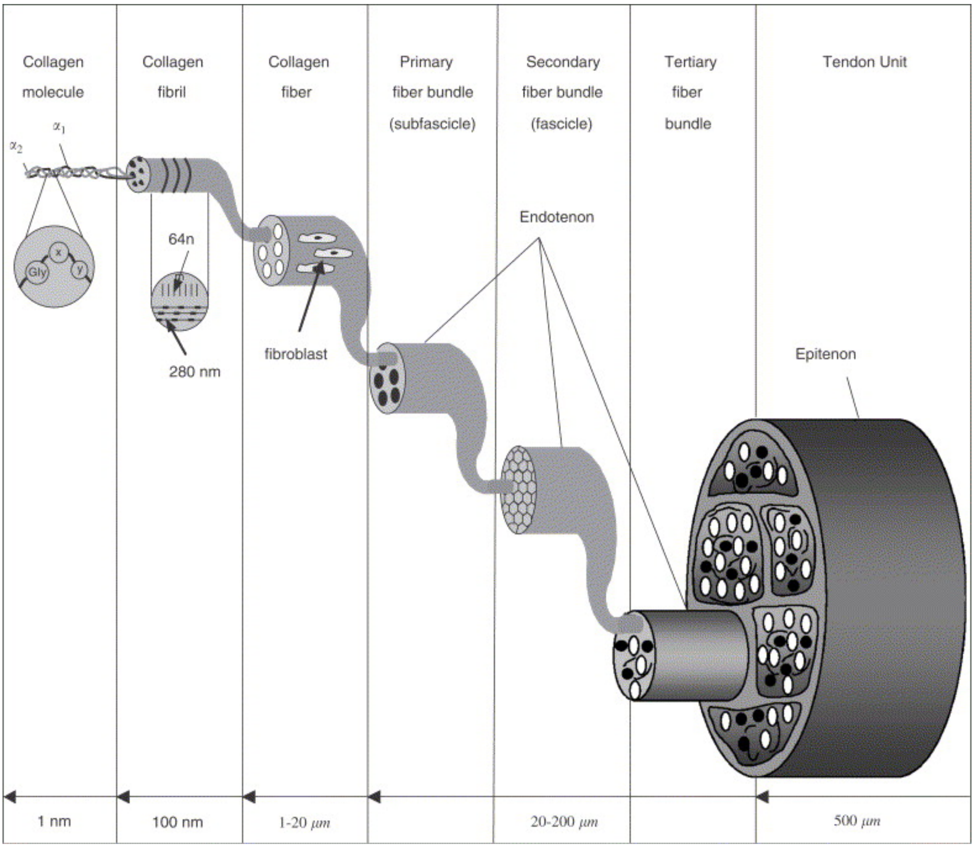

Figure 2: A schematic of a multi-unit hierarchical structure of the tendon [1].

Tendons are rich in collagen accounting for approximately 70% of the dry mass (mainly type I) [3]. Collagen is the main component of the multi-unit hierarchical structure characterizing the tendons (see Fig.2). The fibril is the smallest tendon unit structure mostly built up by tropocollagen triple-helices packed together. The fibrils form fibers that are bundled together in fascicles bond together with blood vessels, lymphatics and nerves by the endotenon, a thin layer of connective tissue. Collections of fascicles are enclosed by the epitenon, which is a loose connective tissue sheath. The hierarchical structure aligns the bundles of fibers along the longitudinal axis of the tendon providing great strength in that direction. Although, at rest the single fibers assume a 'crimp pattern', which gradually disappears as the tendon is increasingly stretched [1]. The properties of the collagen and the organized structure enable the tendon to withstand large forces and also greatly influence the overall behaviour in tension.

The other components constitute the ground substance of the ECM surrounding the collagen. The proteoglycans content varies between 0.2% and 3.5% depending on the mechanical function of the tendon and its role is to attract water and keep the tendon hydrated [1]. Elastin is found in small quantities with the role of recovering the crimped configuration and glycoproteins contributing to the mechanical stability of the tendon [1,18]. Water accounts for approximately 70% of tendon's total weight [18]. The interaction between the water and some of the components of the ECM, particularly glycoproteins, influences the viscoelastic behaviour of the tissue. In addition, water provides lubrication reducing inter-fascicular friction and also acts as medium carrying nutrients to the fibroblasts and taking waste substances out of the tendon [19].

2.2 Mechanical properties of tendons

Tendons undergo dynamic loading in *vivo* that together with the complex structure and interaction between the components yield a characteristic non-linear mechanical response. A tensile load yields the typical stress-strain curve shown in Fig.3. From a rest configuration until 2% stretch the stiffness gradually increases; this initial behaviour is commonly attributed to the gradual recruitment of the fibrils that from the 'crimp pattern' are re-oriented in the direction of the load. This interval is called the 'toe' region. Once the fibers are straighten-up, the tendon reaches its characteristic stiffness, which remains constant within the 'linear' region. If the tendon is stretched further, microscopic failures of the collagen fibers occurs (i.e. ruptures). Further on, macroscopic failures occur resulting in a general softening up until 8-10% when the tendon reaches complete rupture [1].

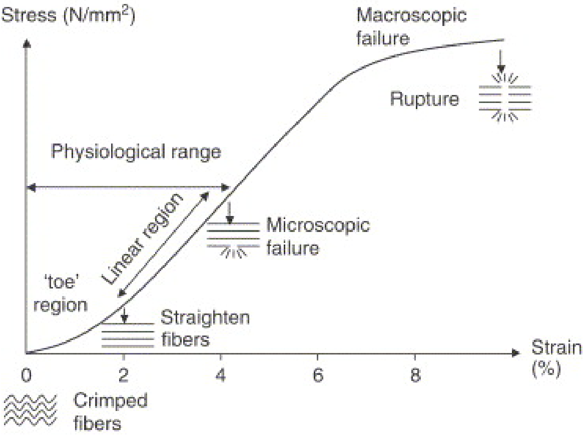

Figure 3: Tendon stress-strain curve under loading along longitudinal axis [1].

In a tensile test, even if the load applied is maintained within the 'toe' region, the tendon does not behave merely elastically. The collagen fibers and the matrix components, indeed, have been demonstrated to posses viscous properties. Thus, tendons show time-dependent behaviour such as creep, stress-relaxation and mechanical hysteresis [20].

The creep behaviour is shown by the variation through time of deformation when a constant force is applied. In tensile tests the elongation increases non-linearly until it reaches a steady-state (Fig.4a). Similarly, stress-relaxation means that the stress required to maintain a constant applied elongation decreases over time until a steady-state is reached (Fig.4b). The mechanical hysteresis, instead, is shown when the response of a tendon to the loading phase of a test follows a different path than a subsequent unloading phase. In a stress-strain curve the hysteresis is the area enclosed between the loading and the unloading curve, which represents the energy lost as heat by the viscous components of the tendon (Fig.4c) [20].

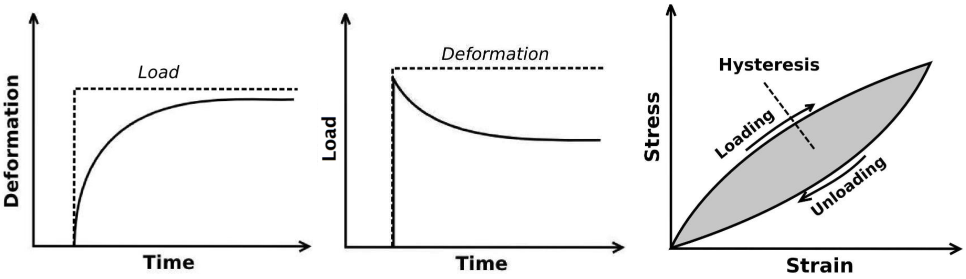

(a) Creep. (b) Stress-relaxation. (c) Mechanical hysteresis.

Figure 4: Viscous behaviours.

2.3 Constitutive models for biological soft tissues

The complex mechanical behaviour of tendons and biological soft tissues in general have been modeled with a considerable number of different constitutive models. The tissues have been modeled mainly by two types of models: continuum models and structural models. The continuum models consider the tissue as a homogeneous material with the same properties throughout. In the structural models, instead, the tissue is seen as a combination of components with different properties, which together determine the overall mechanical behaviour.

The simplest continuum constitutive model is Hooke's linear elastic model for solid materials. This model assumes a linear relationship between stresses and strain, which can be isotropic, orthotropic or anisotropic. This type of model is only valid for describing the material behaviour in the case of small deformations, while the soft tissues normally undergo large deformations in *vivo*, which result in non-linear behaviour [21].

A class of models able to describe non-linearities are the hyperelastic material models. Several theories have been presented of which the most commonly used are neo-Hookean, St.Venant, Arruda-Boyce, Mooney-Rivlin and Ogden [21]. However, these models lack time-dependent components and are unable to describe the characteristic property of soft tissue that is viscoelasticity, expressed by creep, stress relaxation and hysteresis.

Three classic models of this type are Maxwell, Kelvin-Voigt and the Standard Linear Solid (SLS). These are simple one-dimensional models differently composed by combinations of springs as the elastic component and dash pots as the viscous component; hence, viscoelastic models.

A large variety of viscoelastic models have been developed using the quasi-linear viscoelastic theory (QLV) formulated by Fung [22]. In the one-dimensional case, the stress is given by the convolution integral function of time (t) and strain (ϵ)

$$\sigma(t,\epsilon) = \int_0^t G(t-\tau)\frac{\partial\sigma^e}{\partial\epsilon}\frac{\partial\epsilon}{\partial\tau}d\tau \tag{1}$$

where G(t-τ) is the relaxation function and σ^e is the time-independent elastic response [23–25]. Although it has been used successfully to describe the tendon mechanical behaviour [23], it was proven to have limitations in stress-relaxation and creep tests since the dependency of time and strain or stress are separated [26].

In the earliest structural models, collagenous tissue consisted of elastin fibers and undulated collagen fiber altogether interconnected to form an articulated network structure. Both types of fibers were assumed to be linear elastic, but the non-uniform structure resulted in a non-linear response [27].

In later developments the tissue was modelled including also the contribution to the stresses of a fluid matrix embedding the fibers as hydrostatic pressure [28].

A more recently developed type of structural model are the fiber-reinforced models. This type of models has been used successfully to describe articular cartilage [12,13,29]. In these studies the solid matrix (σ_s) consisted of a fibrillar part (σ_{fib}), representing the collagen network and a non-fibrillar part (σ_{nonfib}), the ground substances, which were treated separately but both contributing to the total stress.

$$\boldsymbol{\sigma}_s = \boldsymbol{\sigma}_{fib} + \boldsymbol{\sigma}_{nonfib} \tag{2}$$

In addition a fluid phase was considered as hydostatic pressure (p) giving the total stress (σ_{tot})in the cartilage as

$$\boldsymbol{\sigma}_{tot} = \boldsymbol{\sigma}_{fib} + \boldsymbol{\sigma}_{nonfib} - p\mathbf{I} \tag{3}$$

An interesting aspect of this type of models is that the main components of soft tissues can be represented separately, so their function in the overall structure can be investigated. This could be a considerable advantage for models aiming to simulate more complex behaviours such as failure and healing.

So far limited number of studies have developed models specifically for tendons [30–32] and most of them described the mechanical behaviour only considering the fibrillar part.

The existing model of the Achilles tendon, which this study further develops, was based on a biphasic fiber-reinforced structural model proposed by Wilson and Julkunen for articular cartilage [12,13]. The model was obtained by modifying the collagen network to resemble the Achilles tendon structure [11].

2.3.1 The biphasic fiber-reinforced structural model

In the studies used as main reference for the formulation of the model for the tendon material [33,34], the material was modeled as a fibril-reinforced poroviscoelastic material assumed as biphasic, consisting then of a solid matrix saturated with water [13].

The fibrillar part of the solid phase was composed by a combination of large primary collagen fibrils and smaller secondary fibrils [12,34]. The first were disposed in an arcade manner, while the second randomly distributed throughout the model [12]. The deformation for each fibril was evaluated with the logarithmic strain as [34]:

$$\epsilon_f = log(\lambda) \tag{4}$$

where λ is the elongation defined as

$$\lambda = \frac{\| \mathbf{F} \cdot \mathbf{e}_{f,0} \|}{\| \mathbf{e}_{f,0} \|} = \frac{\| \mathbf{e}_f \|}{\| \mathbf{e}_{f,0} \|} \tag{5}$$

where $\mathbf{e}_{f,0}$ and $\mathbf{e}_f$ are the initial and current fibril length vector respectively and $\mathbf{F}$ the deformation tensor. After deformation the orientation fibril vector was computed as:

$$\vec{e}_f = \frac{\mathbf{F} \cdot \mathbf{e}_{f,0}}{\| \mathbf{F} \cdot \mathbf{e}_{f,0} \|} \tag{6}$$

Then, the fibril stress tensor was given by [35]

$$\boldsymbol{\sigma}_f = \frac{\lambda}{J} P_f \vec{e}_f \vec{e}_f \tag{7}$$

where J is the determinant of the deformation tensor and P_f is the first Piola-Kirchhoff fibril stress [35]. The viscoelastic behaviour of the fibrils was represented using the Standard linear solid model (SLS). That is composed by a spring in parallel (E_1) with another spring (E_2) in series with a dash pot (η), see Fig.5. The mechanical behaviour of the springs was described by two-parameter exponential stress-strain relationships [35]:

$$P_1 = \begin{cases} E_1(e^{k_1\epsilon_f} - 1) & \text{for} \quad \epsilon_f > 0 \\ 0 & \text{for} \quad \epsilon_f \leq 0 \end{cases}$$

and

$$P_2 = \begin{cases} E_2(e^{k_2\epsilon_e} - 1) & \text{for} \quad \epsilon_e > 0 \\ 0 & \text{for} \quad \epsilon_e \leq 0 \end{cases}$$

where ϵ_f and ϵ_e are the strains in the two springs, E_1, E_2, k_1 and k_2 are positive material constants. Note that the fibrils were assumed to resist only tension.

The total stress in the fibril is then

$$P_f = P_1 + P_2. \tag{8}$$

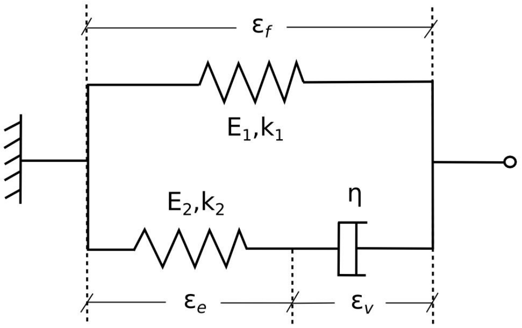

Figure 5: Schematic of the Standard Linear Solid model (SLS).

The non-fibrillar part was described as a compressible neo-Hookean material. The constitutive equations were derived from the energy function [33]:

$$W_{neo} = \frac{K_m}{2}\left(\frac{1}{2}(J^2-1) - ln(J)\right) + \frac{1}{2}G_m\left(tr(\mathbf{C}) - 3det(\mathbf{C})\right) \tag{9}$$

where the $\mathbf{C}$ is the left Cauchy-Green deformation tensor ($\mathbf{F}\mathbf{F}^T$), the bulk modulus is defined as

$$K_m = \frac{E_m}{3(1-2\nu_m)} \tag{10}$$

and the shear modulus

$$G_m = \frac{E_m}{3(1+\nu_m)} \tag{11}$$

where E_m is the Young's modulus and ν_m the Poisson ratio of the matrix. The Cauchy stresses in the matrix were given by

$$\boldsymbol{\sigma}_{neo} = \frac{1}{2}K_m\left(J - \frac{1}{J}\right)\mathbf{I} + \frac{G_m}{J}(\mathbf{B} - J^{2/3}\mathbf{I}) \tag{12}$$

where $\mathbf{B}$ is the right Cauchy-Green deformation tensor ($\mathbf{F}^T\mathbf{F}$).

The contribution of the fluid phase to the total stresses was accounted as hydrostatic pressure as in equation (3). Physically, it expresses the frictional drag caused by the fluid flow, which is believed to be the main cause of the viscoelastic behaviour [36]. Darcy's law is commonly used to describe the fluid flow (Q) given by

$$Q = Ak\frac{\Delta p}{h} \tag{13}$$

states that it is directly proportional to the cross-section area A, the permeability k, the difference in pressure Δp and inversely proportional to the thickness h. The permeability was assumed to depend on the void rations in the tissue [37]:

$$k = k_0\left(\frac{1+e}{1+e_0}\right)^{M_k} \tag{14}$$

where e and e_0 are respectively the current and initial void ratios and M_k a positive constant [37]. The void ratios are defined as

$$e = \frac{n_f}{n_s} \tag{15}$$

where n_s and n_f is the total water volume fraction given by

$$n_f = \frac{\rho_s n_{f,m}}{1 - n_{f,m} + n_{f,m}\rho_s} \tag{16}$$

in which $n_{f,m}$ is the water mass fraction and ρ_s the solid tissue density [34].

2.3.2 St.Venant-Kirchhoff orthotropic hyperelastic material model

In contrast to an isotropic material, which can be defined only by two constants, an orthotropic material requires the definition of 9 independent parameteres: 3 Young's moduli (E_1, E_2, E_3), 3 Poisson ratios (ν_{12}, ν_{13}, ν_{23}) and 3 shear moduli (G_{12} ,G_{13}, G_{23}) [38]. If a linear stress-strain relationship is assumed, the Hooke's law ($\boldsymbol{\sigma} = \mathbf{D}\boldsymbol{\epsilon}$) is valid and the stiffness tensor $\mathbf{D}$ can be written in the matrix form referred to the principal material axes [39]:

$$\mathbf{D} = \begin{bmatrix} a_{11} & a_{12} & a_{13} & 0 & 0 & 0 \\ a_{21} & a_{22} & a_{23} & 0 & 0 & 0 \\ a_{31} & a_{32} & a_{33} & 0 & 0 & 0 \\ 0 & 0 & 0 & 2G_{12} & 0 & 0 \\ 0 & 0 & 0 & 0 & 2G_{13} & 0 \\ 0 & 0 & 0 & 0 & 0 & 2G_{23} \end{bmatrix}$$

where the components a_{ij} $(i, j = 1, 2, 3)$ are given by:

$$a_{ii} = E_i \frac{1 - \nu_{jk}\nu_{kj}}{\Delta} \quad \text{(no sum. over } i\text{)} \tag{17}$$

$$a_{ij} = E_i \frac{\nu_{ji} - \nu_{ki}\nu_{jk}}{\Delta} \quad (i \neq j \neq k) \tag{18}$$

with

$$\Delta = 1 - \nu_{12}\nu_{21} - \nu_{13}\nu_{31} - \nu_{23}\nu_{32} - 2\nu_{12}\nu_{23}\nu_{31} \quad \text{and} \quad \nu_{ij} = \nu_{ji}\frac{E_i}{E_j} \tag{19}$$

In addition the following constraints have to be fulfilled [19]:

$$E_1, E_2, E_3, G_{12}, G_{13}, G_{23} > 0\,, \qquad \Delta > 0 \quad \text{and} \qquad \mid \nu_{ij} \mid < \left(\frac{E_i}{E_j}\right)^{1/2} \tag{20}$$

The behaviour of an orthotropic hyperelastic material can be described by the St.Venant-Kirchhoff strain energy function [39]

$$W_{ort} = \frac{1}{2}\sum_{i,j}^{3} a_{ij} tr(\mathbf{EL}_{ii}) tr(\mathbf{EL}_{jj}) + \sum_{i,j \neq i}^{3} G_{ij} tr(\mathbf{EL}_{ii}\mathbf{EL}_{jj}). \tag{21}$$

where $\mathbf{E}$ is the Green-Lagrange strain tensor

$$\mathbf{E} = \frac{1}{2}(\mathbf{C} - \mathbf{I}) \tag{22}$$

in which $\mathbf{I}$ is the second order identity matrix and $\mathbf{C}$ is the right Cauchy-Green tensor defined as

$$\mathbf{C} = \mathbf{F}^T\mathbf{F} \tag{23}$$

and the tensor $\mathbf{L}_{ii}$ is given by

$$\mathbf{L}_{ii} = \mathbf{l}_i \otimes \mathbf{l}_i \quad (i = 1, 2, 3) \tag{24}$$

where $\mathbf{l}_i$ (i=1,2,3) is a set of orthogonal unit base.
The second Piola-Kirchooff stress tensor is then derived as

$$\mathbf{S} = \frac{\partial W}{\partial \mathbf{E}} = \sum_{i,j}^{3} a_{ij} tr(\mathbf{E}\mathbf{L}_{jj})\mathbf{L}_{ii} + 2 \sum_{i,j \neq i}^{3} G_{ij} \mathbf{L}_{ii}\mathbf{E}\mathbf{L}_{jj} \tag{25}$$

and the Cauchy stress tensor obtained with

$$\boldsymbol{\sigma}_{ort} = J^{-1}\mathbf{F}\mathbf{S}\mathbf{F}^T. \tag{26}$$

2.3.3 Transversely isotropic conditions

A special class of orthotropic materials are the transverse isotropic materials. These materials have same properties in one plane and different in the direction normal to the plane (Fig 6). From the orthotropic case, the corresponding stiffness tensor for transverse isotropic materials is obtained imposing the following additional conditions:

$$E_1 = E_3 = E_p\,, \quad E_2 = E_n\,, \quad \nu_{13} = \nu_{31} = \nu_p\,, \quad \nu_{12} = \nu_{32} = \nu_{pn} \tag{27}$$

$$\nu_{21} = \nu_{23} = \nu_{np}\,, \quad G_{12} = G_{23} = G_{pn} \quad \text{and} \quad G_{13} = \frac{E_p}{2(1 + \nu_p)} \tag{28}$$

where direction 1 and 3 are defined as the 'in plane' direction (p) and 2 the normal direction (n). These conditions reduce the number of independent parameters needed to define the material from 9 to 5.

Models with these properties are commonly used to model fiber-reinforced materials in which the fibers lie along the same direction. Also tendons have been modeled as transversely isotropic earlier by Yin et al. [36] obtaining a satisfactory representation of the mechanical behaviour.

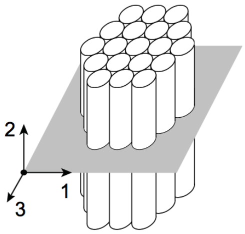

Figure 6: Schematic of a transversely isotropic material.

2.4 Experimental tests and data

In order to validate and assess the ability of the model to simulate the behaviour of the Achilles tendon, experimental data are needed. For the purposes of this project data were obtained from collaborators [17], who tested Achilles tendons of rats under cyclic tensile loading. Measurements from the control group of a tendon experiment consisting of 9 tendons from 16 weeks old female Sprague-Dawley rats were used for this study.

For the experiment the tendons were dissected free from extraneous soft tissue and harvested together with the calcaneal bone and part of the gastrocnemious and soleus muscle complex. During the tissue preparation and mounting in the material testing machine, the tendons were kept moist using gauze with physiological solution. For clamping, the muscle was scraped off the tendon and the fibers were attached between fine sandpaper and fixed in a metal clamp. In the other end of the tendon, the calcaneous bone was fixed at 30^o dorsiflexion relative to traction direction. The samples were set in the material testing machine (100R, DDL, Eden Praine, MN) with the tendon oriented vertically. The tests considered consisted of 20 cycles of tensile pull between 1 and 20 N at a constant speed of 0.1 mm/s [17] (Fig.7). The length and radius of the middle transverse section of each tendon were measured. More details on the experiment and its results can be found in the collaborators' paper [17].

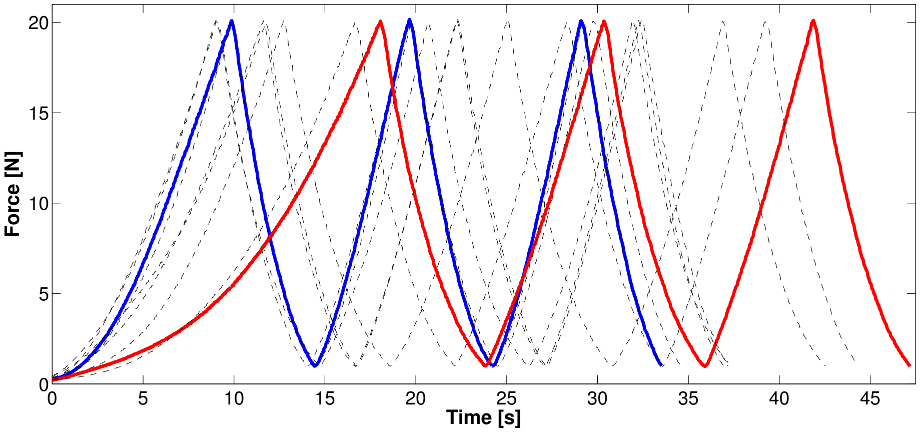

Figure 7: Measured force-time curves of first three cycles of control group tendons. To demonstrate the variation in the experiment tendon 1272 (red line) and 1270 (blue line) were highlighted. These curves correspond to the testes that took respectively the longest and shortest time in the group. The dashed lines correspond to remaining tendons.

3 Methods

3.1 Constitutive models

The Achilles tendon is modeled as the combination of fibrillar, representing the collagen fibers, and non-fibrillar part, the matrix surrounding the fibers. The collagen fibers are assumed to be one-dimensional and to run parallel to the longitudinal axis through the matrix. The viscoelastic behaviour of the fiber is modeled with the standard linear solid model (SLS) with exponential springs. The non-fibrillar matrix is modeled as a biphasic porous material with the solid part fully saturated with water. In this thesis two constitutive models of the matrix are investigated: a compressible isotropic neo-Hookean material model and a St.Venant-Kirchhoff orthotropic material model with transversely isotropic properties.

Modeling the matrix as an orthotropic material allows to investigate the effect of Poisson ratios higher than 0.5, which is a constitutive limit for isotropic materials [19]. This means that the model can simulate a decrease in volume of the tendon under tensile loading instead of an increase. This change is expected to impact the prediction of the fluid behaviour.

3.2 Finite element implementation

The finite element model was implemented in ABAQUS(v6.12-4, Dassault System, France). The option `nlgeom` was used to account for large deformations. Although for this type of deformations the update Lagrangian formulation is preferable, with the option selected correct calculations were obtained adopting the total Lagrangian formulation. This means that the deformation gradient **F** is defined as

$$\mathbf{F}_i = \frac{\partial \mathbf{x}_i}{\partial \mathbf{x}_0} \tag{29}$$

where $\mathbf{x}_0$ is the position vector in the initial configuration and $\mathbf{x}_i$ in the current configuration at the i^{th} iteration step. Same formulation was adopted by Wilson and Julkunen as shown in equation (5) [12, 13].

The total stresses in the tendon were calculated as suggested in the related studies as

$$\boldsymbol{\sigma}_{tot} = \boldsymbol{\sigma}_s - p\mathbf{I} \tag{30}$$

While the hydrostatic pressure p was computed by ABAQUS using predefined functions, the material models of the solid matrix $\boldsymbol{\sigma}_s$ were implemented in the subroutine UMAT, which specifically is set for user-defined material properties. For the calculations the software requires the determination of the Jacobian (${}^4\mathbf{C}$) with the subroutine. As derived by Wilson [33], the Jacobian is equal to

$$^4\mathbf{C} = \frac{1}{J}\left(\boldsymbol{\sigma}_s \frac{\partial J}{\partial \mathbf{F}} + J\frac{\partial \boldsymbol{\sigma}_s}{\partial \mathbf{F}}\right)\mathbf{F}^T \tag{31}$$

where $\mathbf{F}$ is the deformation gradient tensor, J the determinant of $\mathbf{F}$ and $\boldsymbol{\sigma}$ the Cauchy stress tensor. The term $\frac{\partial J}{\partial \mathbf{F}}$ is given by

$$\frac{\partial J}{\partial \mathbf{F}} = \frac{\partial det(\mathbf{F})}{\partial \mathbf{F}} = J\mathbf{F}^{-1}. \tag{32}$$

Therefore, the unknowns in equation (31) are $\boldsymbol{\sigma}_s(\mathbf{F})$ and $\frac{\partial \boldsymbol{\sigma}_s(\mathbf{F})}{\partial \mathbf{F}}$, which depend on the chosen material model. Thus, to investigate the model using a neo-Hookean matrix the following needs to be determined:

$$\boldsymbol{\sigma}_s = \boldsymbol{\sigma}_f + \boldsymbol{\sigma}_{neo} \quad \text{and} \quad \frac{\partial \boldsymbol{\sigma}_s}{\partial \mathbf{F}} = \frac{\partial \boldsymbol{\sigma}_f}{\partial \mathbf{F}} + \frac{\partial \boldsymbol{\sigma}_{neo}}{\partial \mathbf{F}} \tag{33}$$

and similarly for the model with a orthotropic matrix:

$$\boldsymbol{\sigma}_s = \boldsymbol{\sigma}_f + \boldsymbol{\sigma}_{ort} \quad \text{and} \quad \frac{\partial \boldsymbol{\sigma}_s}{\partial \mathbf{F}} = \frac{\partial \boldsymbol{\sigma}_f}{\partial \mathbf{F}} + \frac{\partial \boldsymbol{\sigma}_{ort}}{\partial \mathbf{F}} \tag{34}$$

3.2.1 Fibrillar part

As described in section 2.3.1 the first Piola-Kirchhoff stresses in the springs under tension are given by

$$P_1 = E_1(e^{k_1 \epsilon_f} - 1) \tag{35}$$

$$P_2 = E_2(e^{k_1 \epsilon_e} - 1) = \eta \dot{\epsilon}_v \tag{36}$$

and the total stress

$$P_f = P_1 + P_2 \tag{37}$$

For numerical implementation a solution of equation (37) is needed for every time step. Using equations (35), (36) and (37) with Euler backward time integration it can be derived that the total stresses are given by

$$P_f^{t+\Delta t} = -\frac{b}{2} + \frac{1}{2}\sqrt{b^2 - 4c} \tag{38}$$

where

$$b = E_2 - 2P_1 - \eta\dot{\epsilon}_f + \frac{\eta}{k_2 \Delta t} \tag{39}$$

$$c = -\frac{\eta}{k_2 \Delta t}P_f^t - (P_1 + \eta\dot{\epsilon}_f)(E_2 - P_1) - \frac{\eta}{k_2}\dot{P}_1 \tag{40}$$

$$\dot{\epsilon}_f = \frac{\epsilon^{t+\Delta t} - \epsilon_f^t}{\Delta t} \tag{41}$$

and

$$\dot{P}_1 = E_1 k_1 e^{k_1 \epsilon_f} \dot{\epsilon}_f \tag{42}$$

Complete derivations can be found in Gustafsson's thesis [11].

The Cauchy stresses in the fibril implemented was obtained using equations (5), (6) and (38) into equation (7) giving

$$\boldsymbol{\sigma}_f = \underbrace{\frac{1}{J}\frac{P_f^{t+\Delta t}}{\lambda}}_{\text{A}} \underbrace{\mathbf{F}\mathbf{e}_0\mathbf{e}_0^T\mathbf{F}}_{\mathbf{B}} \tag{43}$$

Hence the second unknown was derived as

$$\frac{\partial \boldsymbol{\sigma}_f}{\partial \mathbf{F}} = \mathbf{B}\frac{\partial A}{\partial \mathbf{F}} + A\frac{\partial \mathbf{B}}{\partial \mathbf{F}} \tag{44}$$

Further calculation of these derivatives are shown in the appendix.

3.2.2 Neo-Hookean material

For the implementation of the neo-hookean material, the Cauchy stresses is given by equation (12) and its derivative with respect to the deformation tensor was derived by Wilson [33] as

$$\frac{\partial \boldsymbol{\sigma}_{neo}}{\partial \mathbf{F}} = \left[\frac{1}{2}K_m\mathbf{I}\left(1+\frac{1}{J^2}\right) - \mathbf{B}\left(\frac{G_m}{J^2}\right) + \frac{G_m}{3J^{4/3}}\mathbf{I}\right] J\mathbf{F}^{-1} + \frac{G}{J}2[{}^4\mathbf{I}\mathbf{F}^T] \tag{45}$$

where ${}^4\mathbf{I}$ is the forth order symmetric identity matrix.

3.2.3 Orthotropic hyperelastic material

The Cauchy stresses in an orthotropic hyperelastic matrix were implemented as shown in section 2.3.2 by equation (26). The derivation of the second term needed to define the Jacobian is then obtained as follow:

$$\frac{\partial \boldsymbol{\sigma}_{ort}}{\partial \mathbf{F}} = \frac{\partial}{\partial \mathbf{F}}\left(J^{-1}\mathbf{F}\mathbf{S}\mathbf{F}^T\right) = -\frac{\mathbf{F}\mathbf{S}\mathbf{F}^T}{J^2}\frac{\partial J}{\partial \mathbf{F}} + \frac{\partial \mathbf{F}}{\partial \mathbf{F}}\frac{\mathbf{S}\mathbf{F}^T}{J} + \frac{\mathbf{F}}{J}\frac{\partial \mathbf{S}}{\partial \mathbf{F}}\mathbf{F}^T \tag{46}$$

where the first derivative of the right hand side is known (see equation (32)) and the second was defined as

$$\frac{\partial \mathbf{F}}{\partial \mathbf{F}} = {}^4\mathbf{I} \tag{47}$$

The last derivative was derived using the chain rule yielding

$$\frac{\partial \mathbf{S}}{\partial \mathbf{F}} = \frac{\partial \mathbf{S}}{\partial \mathbf{E}}\frac{\partial \mathbf{E}}{\partial \mathbf{F}} \tag{48}$$

where the constant elastic tensor was derived by Itskov [39] to be

$$\frac{\partial \mathbf{S}}{\partial \mathbf{E}} = \sum_{i,j}^{3} a_{ij} \mathbf{L}_{ii} \times \mathbf{L}_{jj} + 2 \sum_{i,j \neq i}^{3} G_{ij} \mathbf{L}_{ij} \times \mathbf{L}_{ij} \tag{49}$$

which according to tensor calculation rules [39], it can be rewritten as

$$\frac{\partial \mathbf{S}}{\partial \mathbf{E}} = \sum_{i,j}^{3} a_{ij} \mathbf{H}_{ijji} + \frac{1}{2} \sum_{i,j \neq i}^{3} G_{ij} \left[\mathbf{H}_{iijj} + \mathbf{H}_{jiji} + \mathbf{H}_{ijij} + \mathbf{H}_{jjii} \right] \tag{50}$$

where we defined

$$\mathbf{H}_{ijkl} = \mathbf{l}_i \otimes \mathbf{l}_j \otimes \mathbf{l}_k \otimes \mathbf{l}_l \tag{51}$$

The second term is here derived as

$$\frac{\partial \mathbf{E}}{\partial \mathbf{F}} = \frac{\partial}{\partial \mathbf{F}} \left[\frac{1}{2} \left(\mathbf{C} - \mathbf{I} \right) \right] = \frac{1}{2} \left(2 \frac{\partial \mathbf{F}}{\partial \mathbf{F}} \mathbf{F}^T \right) = {}^4\mathbf{I}\mathbf{F}^T \tag{52}$$

Hence, using equations (50) and (52), equation (48) written explicitly becomes

$$\frac{\partial \mathbf{S}}{\partial \mathbf{F}} = \left[\sum_{i,j}^{3} a_{ij} \mathbf{H}_{ijji} + \frac{1}{2} \sum_{i,j \neq i}^{3} G_{ij} \left[\mathbf{H}_{iijj} + \mathbf{H}_{jiji} + \mathbf{H}_{ijij} + \mathbf{H}_{jjii} \right] \right] : {}^4\mathbf{I}\mathbf{F}^T \tag{53}$$

where ':' denotes the double inner product between the tensors. For the implementation of equations (26) and (46), equations (25) and (50) were written simplified in index notation:

$$S_{ij} = \begin{cases} \sum_j^3 a_{ij} E_{jj} & \text{for} \quad i = j \\ 2G_{ij} E_{ij} & \text{for} \quad i \neq j \end{cases}$$

and

$$\left(\frac{\partial \mathbf{S}}{\partial \mathbf{E}} \right)_{klmn} = \begin{cases} a_{kl} & \text{if} \quad (k = n \;\&\; l = m) \\ \frac{1}{2} G_{lm} & \text{if} \quad (k = l \,\&\, m = n \,\&\, k \neq m) \; or \; (k = m \,\&\, l = n \,\&\, k \neq l) \end{cases}$$

where $i, j, k, l, m, n = 1, 2, 3$.

Note that in all derivations the deformation gradient **F** was assumed to be symmetric. Although generally not true, in the loading case considered this assumption is valid and makes the derivations and, thus, the implementation easier.

3.2.4 2D implementation of constitutive formulations

The derivations of the constitutive equations shown previously consider all three dimensions and so they can be applied on the 3D geometry case. To compare the 2D to the 3D geometry case plain strain condition had to be applied. This condition assumes the strains in the out-of-plain direction to be zero. In other words, this assumption allows to disregard certain components of the stiffness matrix that are related to that direction. Therefore, the stiffness matrix, which in the 3D has the same number of non-zero components as in section 2.3.2, becomes

$$\mathbf{D}_{plain} = \begin{bmatrix} C_{1111} & C_{1122} & 0 & 0 & 0 & 0 \\ C_{2211} & C_{2222} & 0 & 0 & 0 & 0 \\ C_{3311} & C_{3322} & 0 & 0 & 0 & 0 \\ 0 & 0 & 0 & C_{1212} & 0 & 0 \\ 0 & 0 & 0 & 0 & 0 & 0 \\ 0 & 0 & 0 & 0 & 0 & 0 \end{bmatrix}$$

where C_{ijkl} are components of the Jacobian ${}^4\mathbf{C}$.

3.3 Average tendon

The tendons used in the experimental tests produced responses quite different between each other even though the same loading conditions were applied (see Fig.7). Differences in the geometric properties of the tendons influence the outcome, as well as the differences in the material properties between individuals that are easily encountered for such biological tissues [17]. Furthermore, inevitable experimental variability due to testing machine and fixation may have influenced the outcome of the tests.

Due to the large variability in both geometry and mechanical response of the tendons, it was of interest to create an average tendon representing the entire population. It was not possible to obtain reasonable data by taking the average because of the large variability cycles' time length. Therefore, each cycle of the data was separately scaled over a period of 2π, then average values of the forces were calculated (Fig.8). At last each cycle of the average curve was rescaled over periods of time calculated as average for each specific cycle of the group. The dimensions of the average tendon were calculated as the mean dimensions of the population. These calculations were implemented and used earlier for the analysis of the existing two-dimensional model [11].

Since the optimization of the model parameters of one tendon required more than a week to complete, only the parameters for the calculated average tendon were optimized.

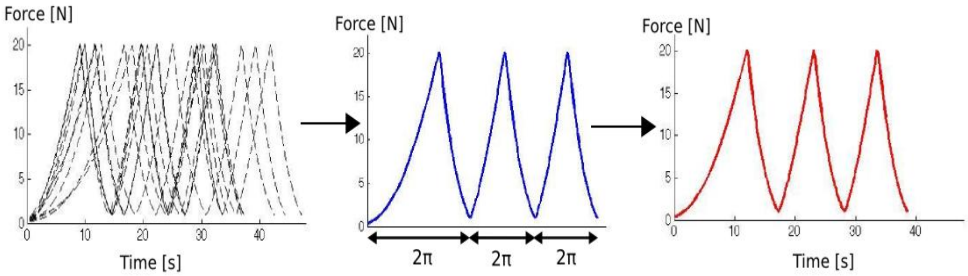

Figure 8: Schematic of calculation of average tendon Force-time curve.

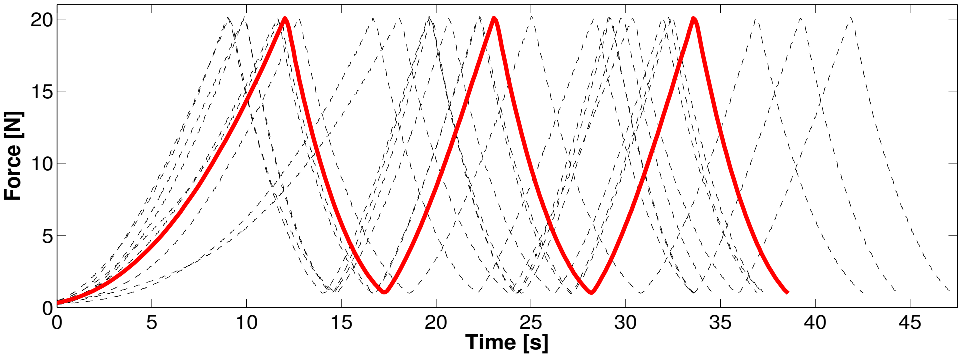

Figure 9: Time-force curves of the calculated average tendon (red line) and of the tendons of the control group (black dashed lines).

3.4 3D geometry, mesh and boundary conditions

The tendon is assumed to have a cylindrical shape. The finite element mesh was created dividing the cylinder in 44 even layers along the height (i.e. length of the tendon), each layer composed of 48 elements. Hence, the mesh consisted of 2112 elements counting a total of 2565 nodes. The type of element chosen was C3D8P, that is 8-node hexahedral poroelastic element.

Boundary conditions were imposed to represent the experiment. The nodes at the bottom were constrained allowing no displacement in any direction and pore pressure set equal to zero on the lateral external surface.

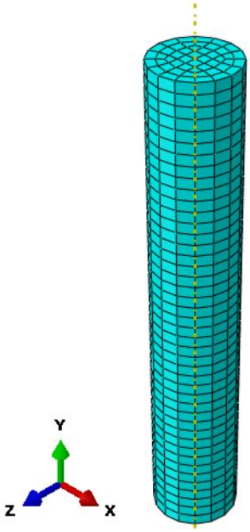

Figure 10: 3D mesh

The loading protocol in the experiment was mimicked by imposing controlled displacement in the y-direction on the nodes at the top. Of the entire set of cycles composing the experimental tests, only the data from the first three cycles were used in the simulations. Figure 11 shows the time displacement curve of the mechanical test. For the numerical calculations each cycle was divided in a lengthening and a shortening step. In addition, a prestrain step was added to obtain the initial conditions of the experiment. The time of this step was calculated knowing the rate of displacement.

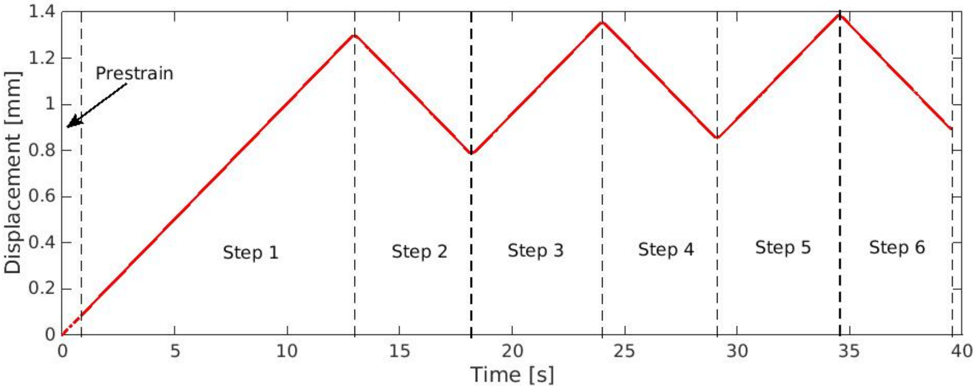

Figure 11: Time-displacement curve with step subdivision used for numerical analysis.

3.5 2D geometry, mesh and boundary conditions

Given the geometry of the 3D case, it is possible to reduce it to a 2D geometry with appropriate approximations. Indeed, the cylindrical mesh can be represented by a rectangular mesh with half the size of the middle sagittal cross section of the cylinder (see Fig.12a). A complete revolution of the rectangle around the longitudinal axis yields the initial cylinder. In the same fashion, for the numerical calculations, the elements and nodes of the rectangular mesh represent integrations over 360^o around the axis of symmetry. Note that this imply the coordinate system to change from Cartesian to cylindrical.

The mesh consisted of 255 nodes and 200 elements of same size ordered in 50 rows of 4 elements each. The type of element chosen is CAX4P, that is 4-node quadratic, axisymmetric and poroelastic element [11].

The boundary conditions were set similarly to the 3D case with the difference that one lateral side became the axisymmetric boundary and on the other the pore pressure was set to zero [11] (see Fig.12b).

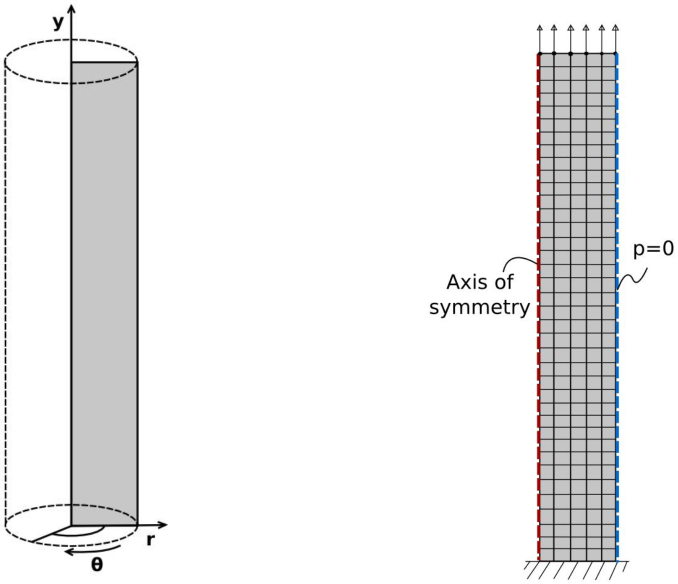

(a) (b)

Figure 12: (a) 2D geometry and approximation. (b) Mesh and boundary conditions.

3.6 Porosity

The tendons used in the experimental study by Eliasson et al. [17] were measured to have a mean dry weight of 24 mg and a water content of 71 mg, which means 75% water mass fraction [17]. Using equation (16), the total water volume fraction was calculated to be 0.834. The density of the dry mass was calculated as $\rho_s = 1.68 g/ml$ knowing the fraction of dry weight and the volume.

3.7 Optimization

Every simulation in ABAQUS took as inputs a set of parameters describing the model and the time-displacement curve. It computed as output the reaction forces generated at the bottom boundary over time. According to the basic laws of mechanics, to have equilibrium in the system the reaction forces produced by the tendon have to be the same as the external forces produces by the machine, which were measured in the experiments. The mean squared error between the simulated and the experimental reaction forces was the objective function minimized by the optimization procedure [40]:

$$f = \frac{1}{6}\sum_{i=1}^{6}\frac{1}{n_i}\left(\sum_{j=1}^{n_i}((F_{mod})_j - (F_{exp})_j)^2\right) \tag{54}$$

where F_{mod} and F_{exp} are respectively the simulated and the experimental reaction forces and n_i is the number of data points for the i^{th} step. Note that the prestrain was not included as it was not measured in the experimental data.

Therefore, the material models were fitted to the experimental data by optimizing the material model parameters. The model with a neo-Hookean matrix had 9 parameters $(E_1, E_2, k_1, k_2, \eta, k_0,\ M_k,\ E_m,\ \nu_m)$, while with a transversely isotropic matrix 12 parameters $(E_1,\ E_2,\ k_1,\ k_2,\ \eta,\ k_0,\ M_k,\ E_p,\ E_n,\ \nu_{pn}, \nu_p, G_{pn})$. Starting from an initial guess the set of parameters, a non-linear unconstrained optimization algorithm (`fminsearch`) in MATLAB was used to minimize equation (54). Convergence was considered to be reached when an increase (or decrease) of the parameters values of 10^{-3} or lower corresponded a variation smaller than 10^{-4} of the objective function f. A schematic of the optimization procedure is shown in Fig. 13.

At last, the optimized curve was evaluated by the root mean square (RMS):

$$\text{RMS error} = \sqrt{\frac{\sum_{j=1}^{n}((F_{mod})_j - (F_{exp})_j)^2}{n}} \tag{55}$$

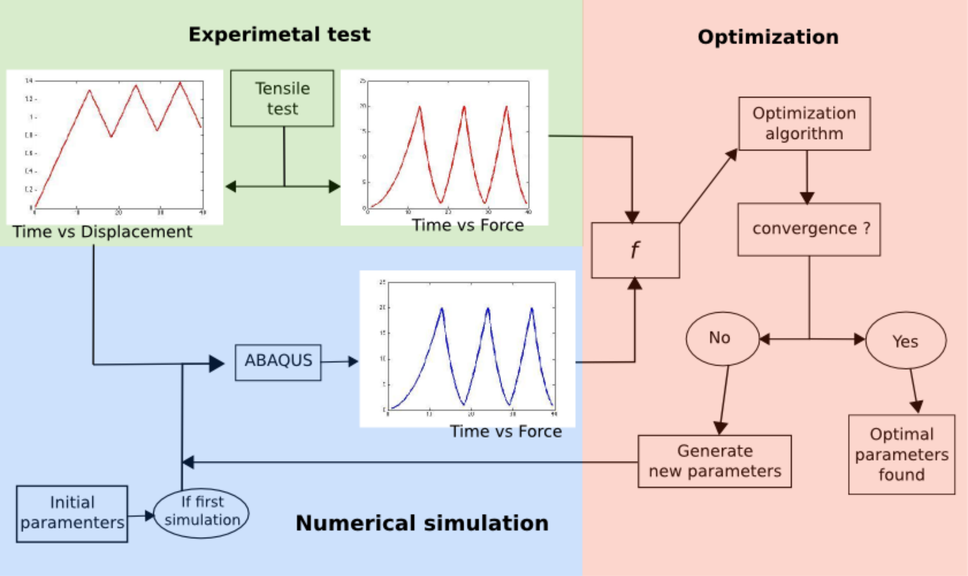

Figure 13: Schematic of the optimization process. For the first numerical simulation the time-displacement curve measured in the experimental test and the initial guessed set of parameters were given to ABAQUS to obtain the simulated reaction forces to compare to the experimental reaction forces. Then the error is calculated by the objective function f. The optimization algorithm continues launching new simulations with new set of parameters until the terms of convergence are met.

Note that to obtain convergence in the single simulations and also for the entire optimization process, the initial set of parameters needed to provide already a decent fit to the experimental data. Furthermore, the several different initial sets have been tried to assess whether the actual optimal sets for the models were obtained.
The range of the parameters values investigated was chosen to be in accordance to those used with the previous work [11].

4 Results

Both constitutive models investigated were able to capture the mechanical behaviour of the average rat Achilles tendon under cyclic loading. The root mean square (RMS) error of the 2D model with neo-hookean matrix (2D neo), the 3D model with neo-hookean matrix (3D neo) and 3D model with transversely isotropic matrix (3D tra) were 0.845, 0.849 and 0.961 respectively. The predictions of the models were quite accurate in the range of forces between 5 and 17 N, but outside this rage the reaction forces tended to be overestimated (see Fig.14). The overestimation was the highest at the peaks and at the end of the cycles (see Table 1, Fig.15b and Fig.15c).

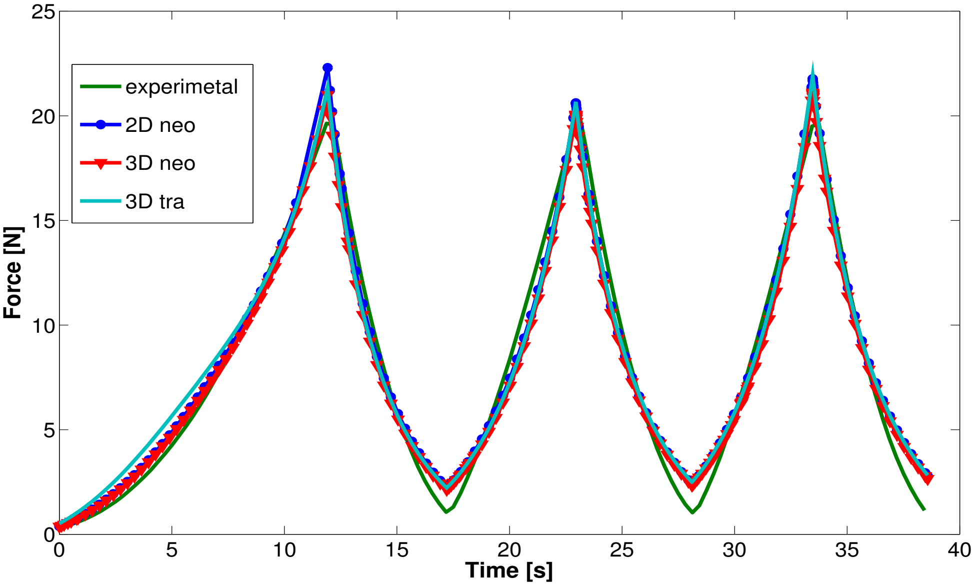

Figure 14: Reaction forces behaviour over time of the average tendon (experimental), 2D model with neo-hookean matrix (2D neo) and the 3D model with neo-hookean matrix (3D neo).

	1^{st} peak	End cycles
2D neo-Hookean	2.66	1.65
3D neo-Hookean	1.36	1.51
3D transversely iso.	1.39	1.68

Table 1: Overestimation in Newtons of the models at the first peak at the end of the last cycle. These correspond to the highest overestimation of the experimental reaction forces.

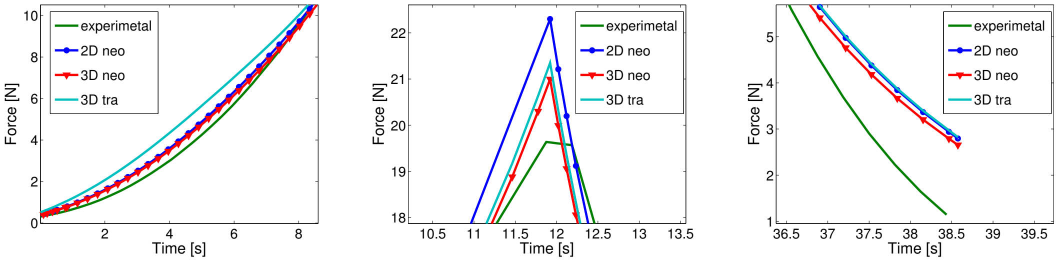

(a) Beginning first cycle.
(b) First peak.
(c) End last cycle.

Figure 15: Parts of reaction forces over time.

Comparing only the models predictions, differences are mostly at the beginning of the first cycle (Fig.15a) and at the first peak (Fig.15b). However they differ by 1.30 N at the most. After the first peak the predictions are almost identical.

The reaction force predictions showed in Fig. 14 were given by the sets of parameters obtained by the optimization procedure giving the lowest RMS error (see table 2). In light of the very similar prediction, it is interesting to compare the parameters' values between models. It can be noticed that the parameters describing the fibrillar part (E_1, E_2, k_1, k_2 and η) are relatively similar (see table 2), while the rest of the parameters describing the permeability (k_0 and M_k) and the matrix show large differences (see table 3).

	RMS	E_1 [MPa]	E_2 [MPa]	k_1	k_2	η [MPa· s]
2D neo	0.857	0.023	0.443	40.00	31.06	609.34
3D neo	0.849	0.023	0.517	40.27	30.40	642.28
3D tra	0.961	0.020	0.556	41.25	32.08	523.51

Table 2: Optimized sets: parameters describing fibrillar part of the 2D model with neo-Hookean matrix (2D neo), the 3D model with neo-Hookean matrix (3D tra) and 3D model with transversely isotropic matrix.

	k_0 [mm/s]	M_k	E_m [MPa]	ν_m			
2D neo	$1.19 \cdot 10^{-7}$	0.96	0.77	0.35	[11]		
3D neo	$0.91 \cdot 10^{-9}$	0.76	0.73	0.41			
	k_0 [mm/s]	M_k	E_p [MPa]	E_n [MPa]	ν_{pn}	ν_p	G_{pn} [MPa]
3D tra	$1.26 \cdot 10^{-9}$	0.38	0.31	2.58	0.14	0.35	0.29

Table 3: Optimized sets: parameters describing permeability and non-fibrillar part of the 2D model with neo-Hookean matrix (2D neo), the 3D model with neo-Hookean matrix (3D tra) and 3D model with transversely isotropic matrix

4.1 Effects of 3D formulation

To investigate the effects of the change in formulation on the prediction of the mechanical behaviours, the tendon was simulated by the 3D neo using the optimal set of parameters for the 2D neo (see Tables 2 and 3) and the results of these two simulations compared.

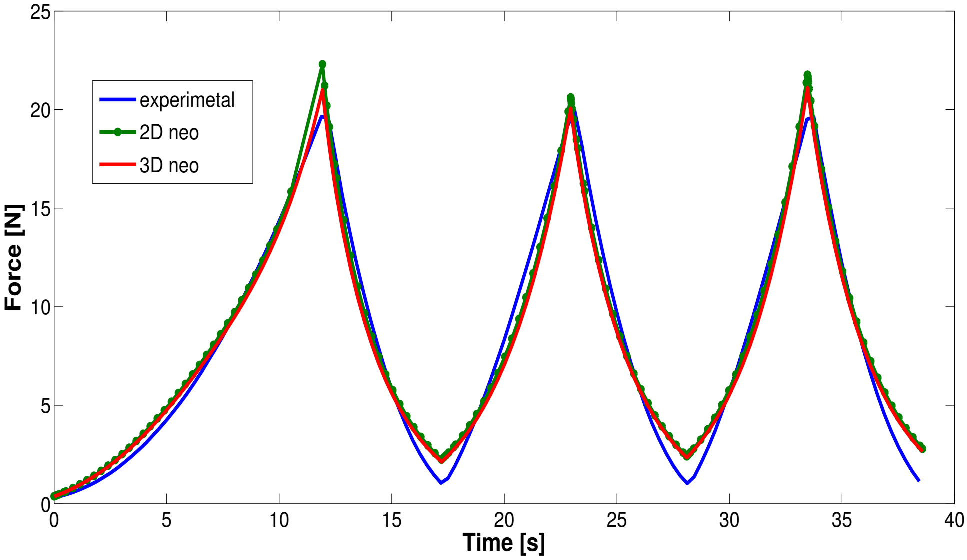

Figure 16: Reaction forces of the average tendon (experimental), the 2D model with neo-hookean matrix (2D neo), the 3D model with neo-hookean matrix (3D neo) and the 3D model with transversely isotropic matrix (3D tra).

The resulting reaction forces is almost identical throughout the simulation indeed the new RMS for the 3D neo was 0.921. The only noticeable difference is on the peak of the first cycle of, where the 2D model predict a force 1.3 N higher (Fig.16). The reason of this difference was found comparing the stresses inside the tendon which are slightly higher in 2D neo (Fig.17a). Moreover, the difference is almost entirely given by the stresses on the fibrillar part, while those on the non-fibrillar part are identical (see Fig.17b-17c). Even more interesting is to notice the subdivision of the stresses in the solid phase. At the peak of the first cycle the fibers support 99.2% of total stresses in the tendon. Even smaller contribution to the total stress is given by the hydrostatic pressure, which accounts for 0.07% of the total (Fig.17d). This is probably the reason why a large variability of values describing permeability and the matrix behaviour do not seem to influence the fit of the reaction forces, while the parameters describing the fibrillar part seem closely related. Also for the hydrostatic pressure the 2D neo estimates higher values than 3D neo.

Note that the stresses presented were calculate in one element on the edge at mid height. However, the stresses were rather homogeneous throughout the geometry and the cycles, so this behaviour can be considered valid for the entire tendon.

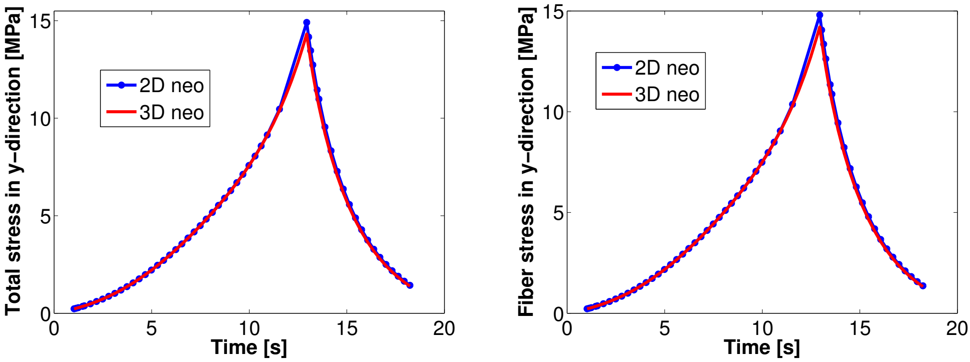

(a) Total stress.

(b) Stress on fibers.

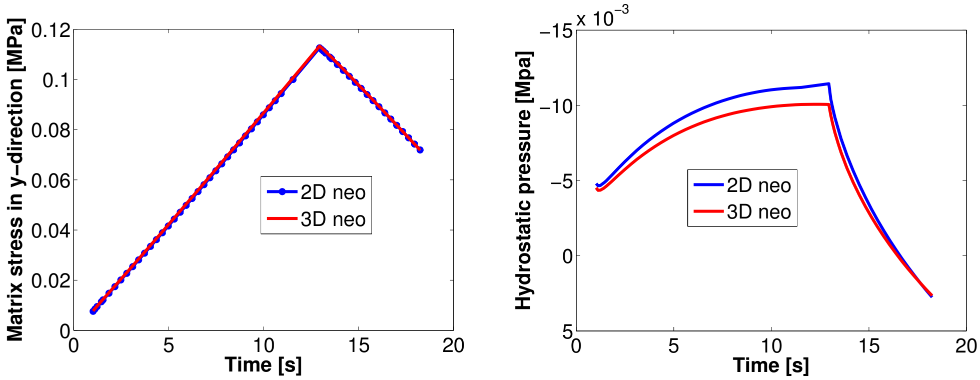

(c) Stress on matrix.

(d) Hydrostatic pressure.

Figure 17: Stresses calculated in an element on the edge at mid height for the first cycle of the 2D model with neo-hookean matrix (2D neo) and the 3D model with neo-hookean matrix (3D neo).

The fluid behaviour was investigated in terms of fluid velocity and flux. The change in geometry had no effect on the fluid velocity (Fig.18a) and on the flux only a slight increase is obtained but the behaviour is completely analogous (Fig.18b).

Note that a positive flux means an inward fluid flow and a negative vice versa.

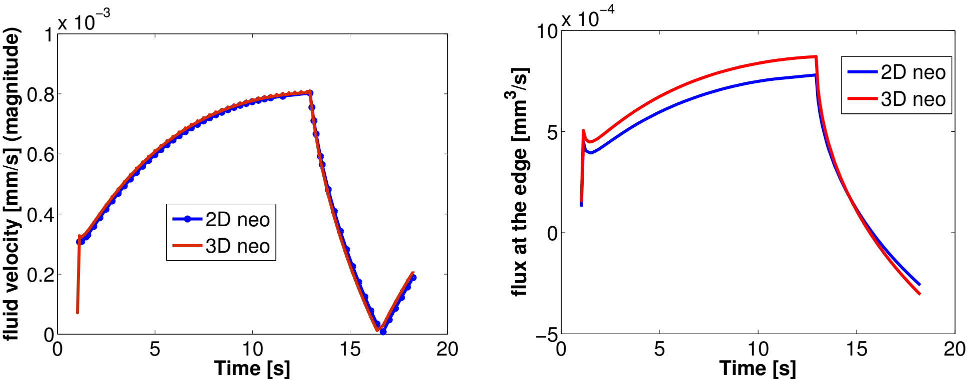

(a) Fluid velocity.

(b) Flux.

Figure 18: Fluid behaviour on the edge at mid height for the first cycle of the 2D model with neo-hookean matrix (2D neo) and the 3D model with neo-hookean matrix (3D neo).

4.2 Effects of different matrix models

The differences of mechanical behaviour between a model with neo-hookean matrix (neo) and transversely isotropic matrix (tra) were also investigated. The 3D models were chosen for the comparison with the results obtained using the respective optimized sets of parameters shown in table 2.

In this case the differences between the models are more noticeable. The total stress in the 3D tra is higher than the 3D neo (Fig.19a). The difference is again mostly given by stress on the fiber, but the matrix has a relatively higher contribution of 5.25% of the total stress at the peak of the first cycle (Fig.19b-19c). Even more significant is the effect on the hydrostatic pressure which, other than reaching 45 times higher values, gives an opposite contribution (Fig.19d). This reversed behaviour is seen in a negative flux that means an outward fluid flow (Fig.20b). Another difference is the variation of fluid behaviour over time, which during tensile load produces a linear variation with the 3D tra instead of non-linear with the 3D neo.

These behavioural differences find an explanation in the differences in parameters values between the two models. In the 3D tra the matrix in the longitudinal direction (E_n) is more than 3 times stiffer than in the 2D neo (E_m)(see table.2), which partly explains the increase of stress taken by the matrix. Moreover the difference between longitudinal (E_n) and 'in plane' (E_p) stiffnesses yields a Poisson ratio of 1.16 relating the stresses in the longitudinal direction and the strains in the lateral direction (ν_{np}). In other words it results in a decrease in volume in the loading phases generating outward fluid flows.

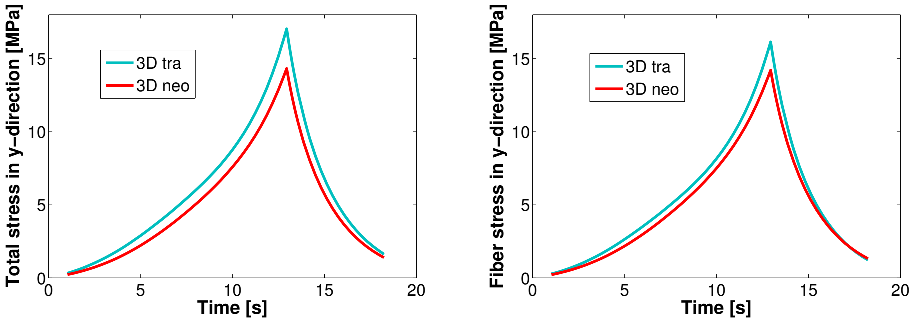

(a) Total stress.

(b) Stress on fibers.

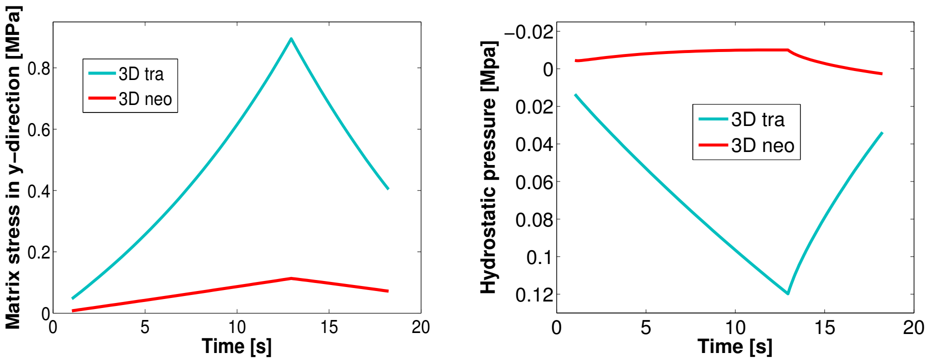

(c) Stress on matrix.

(d) Hydrostatic pressure.

Figure 19: Stresses calculated in an element on the edge at mid height for the first cycle of the 3D model with neo-hookean matrix (3D neo) and 3D model with transversely isotropic matrix (3D tra).

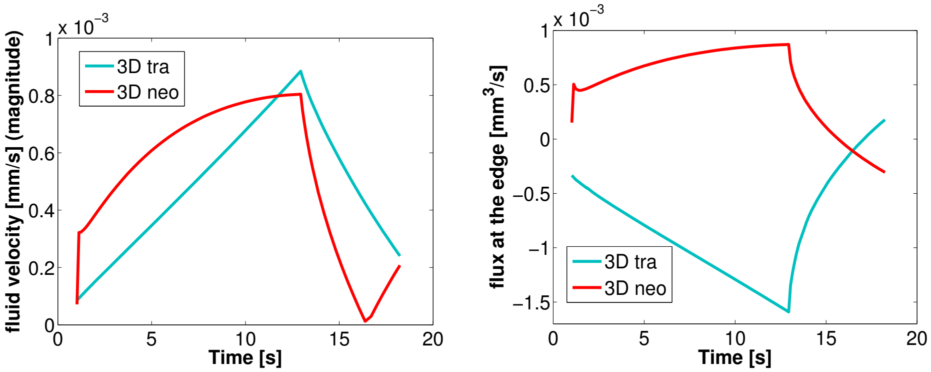

(a) Fluid velocity.

(b) Flux.

Figure 20: Fluid behaviour on the edge at mid height for the first cycle of the 3D model with neo-hookean matrix (3D neo) and 3D model with transversely isotropic matrix (3D tra).

5 Discussion

This study has developed two aspects of a computational model of the Achilles tendon. First the material model formulation has been modified from 2D to 3D to obtain a model that could be applied on a more realistic tendon geometry. Second the constitutive model of the non-fibrillar matrix has been modified to be able to simulate a physiological direction of the fluid flow. The results investigated the effects of the modifications of the model.

5.1 Comparison 2D vs 3D geometry

The comparison between the results of 2D neo and 3D neo showed almost identical behaviour of the two models. Therefore, the modification implemented did not influence the predictions of the material behaviour. Only few small differences in the prediction of the reaction forces and the flux were observed. These differences are most probably given by the numerical calculations that distinguish the 2D from the 3D. Thus, also the geometrical approximations introduced passing from 2D to 3D did not have a significant influence on the predictions.

In this aspect the 2D is more advantageous than the 3D model because the computational time is largely reduced. A simulation of loading case studied applied on the 2D model was computed approximately 20 times faster than on the 3D model. In terms of time it means going from taking less than a minute to more than 15 minutes. Moreover, considering an entire optimization routine, which requires from 600 to 1200 iterations in MATLAB, the difference in computation time becomes a critical factor. However, this advantage is relevant when idealized geometries, such as those of this study, are used.

If we consider a real 3D geometry of an Achilles tendon, it is reasonable to assume that a 2D approximation would introduce more significant differences in the simulated material behaviours. In this situation the 3D model is more proper to use than the 2D model, because it can be applied on any real geometry without introducing further approximations. In fact, irregular (i.e. real) shapes can significantly influence the distribution of stresses inside the tendon. This agrees with a study published by Shim et al. [42], which showed the importance of tendon geometry in determining rupture locations related to cross-sectional areas.

5.2 Comparison isotropic vs transversely isotropic matrix

The fluid behaviour has been suggested to contribute considerably to the viscoelasticity of tendons [36]. A disadvantage of the isotropic model was the prediction of non-physiological fluid behaviour, primarily in terms of direction of flow. Han et al. [14] observed in experimental tensile loading that water was extruded from the inside of the tendon. Instead, the existing model was predicting an increasing inward fluid flow during tension and a decreasing inward flow until outward flow during unloading. Although the fluid behaviour has rather little influence on the overall mechanical behaviour investigated with this model, having a model able to predict a physiological fluid flow is thought to be a needed improvement for later developments. Indeed the fluid flow may play an important role in the cell function and thus indirectly influence the healing process [36]. This objective was successfully fulfilled by substituting the isotropic matrix with a transversely isotropic matrix. The results showed the ability of this model to capture an increasing outward flow during tension and decreasing during unloading. However, the magnitude of water exiting the tendon and its variation over time of the fluid flow could not be confronted to experimental data, because none was available.

Transversely isotropic models have been used before to describe the tendon mechanics. However, these models considered the tendon either as a continuum [43] or as a biphasic material in which the solid phase was not further subdivided [36]. In this study it is assumed that the anisotropic behaviour of the Achilles tendon is given not only by the fibers along the longitudinal direction, but also by the matrix properties. This assumption could not be confirmed nor contradicted since the mechanical properties of the matrix alone has not been clarified yet [44].

In any case, the use of a transversely isotropic matrix may be justified by the simplifying assumption of having straight longitudinally aligned fibers. Indeed in human Achilles tendons the fibers are rotated around each other resulting in a spiraling shape [45]. This complex orientation of the fibers may have an effect on the macroscopic behaviour of the tendon resulting in a decrease of volume and in the characteristic fluid flow. Therefore, introducing the transverse isotropic matrix may help in the shortcoming of the fibrillar model.

5.3 The method

A common problem for models with a large number of parameters is the difficulty in associating a physical meaning to each parameter. The constants of the models used in this study instead can easily be related to the specific parts of the tendon modeled: water, collagen fibers and proteoglycan matrix. However, the method implemented in this study only partially takes advantage of these rather elaborated models. Indeed, the method is able to validate precisely only the fibrillar part of the models with the experimental data available. The experimental data described the reaction forces developed by the tendons during the tensile tests, which can easily be related only to stresses. As shown in the results the stresses were supported almost entirely by the collagen fibers, so the other parts, giving a smaller contribution, receive a much less accurate validation. Certainly, incorporating in the validation experimental data describing specifically the fluid behaviour and mechanical properties of the matrix alone could help obtaining more reliable validation. Though, it has to be pointed out that performing experiments to measure such data requires rather complicated techniques and therefore are rare, if any exists. However, the fact that the models were able to integrate the main components of tendons and that the overall mechanical behaviour could be related to the specific behaviour of each component is an essential starting point for a thorough analysis of the mechanical behaviour of the Achilles tendon.

More in general, given the RMS obtained, the ability of the method used in this study including both the constitutive model and the optimization procedure can be considered satisfactory representing cyclic loading of the Achilles tendon. However under some aspect this method have shown limitations and room for improvements.

For all three models the optimization procedure was tried starting with different sets of initial parameters. In some cases it was observed that the algorithm converged to RMS values (0.85 - 0.96) similar with each other and also close to the best calculated, but resulting from different "optimal" sets. This means that the optimization is not able to provide a unique solution, which is thought to be the consequence of two co-operating factors. First, the optimization algorithm, the MATLAB function `fminsearch`, is very sensitive to the initial values, meaning that it more likely converge to a local minima rather than the global minimum. Second, the models are probably described by an excessive number of parameters (9 and 12). For models of this complexity validated only by measured reaction forces, a high number of parameters can be a limitation in searching for the optimal set. Therefore, a straight forward solution to obtain a better optimization could be to use another algorithm. Another option could be to optimize fewer parameters either by imposing fixed values to those influencing less significantly the optimization outcome (i.e. reaction forces), such as those defining fluid and matrix behaviour.

Finally, a fundamental assumption made in this model is that the fibers are longitudinally oriented. This is a reasonable assumption when the tendon is in the 'linear' region, but it is incorrect in the 'toe' region where the fibers actually assume a 'crimp' pattern. The transition between these two configurations of the fibers is called fiber recruitment, which is mainly responsible for the non-linear behaviour of tendons when stretched from an unloaded state. To represent this behaviour the fibers were assumed to have an exponential relationship between stresses and strains. With this assumption the model is able to give good predictions, but it is a limiting factor in cyclic loading because after the first cycles the tendon tends to remain in the 'linear' region. This is probably the reason of the overestimations of the reaction forces observed in all the models. Therefore, incorporating fiber recruitment would probably improve the predictions. This phenomenon has been modeled before either by modelling a gradual straightening of the fibers with randomly distributed orientations [41] or represented with probability functions [30].

6 Conclusions

In this study an existing two-dimensional isotropic poroviscoelastic model of the Achilles tendon has been further developed in the geometry and in the constitutive model to obtain a three-dimensional transversely isotropic poroviscoelastic model.

The results have shown that the model can be applied on a three-dimensional geometry maintaining accurate representation of the mechanical behaviour of the tendon under cyclic loading. Moreover, modeling the matrix with transversely isotropic properties successfully captures the physiological direction of the fluid flow.

7 Future developments

The ability of the present model to represent the Achilles tendon viscous behaviours could also be investigated with tests like creep and stress-relaxation. Interesting would be to compare its predictions with those of the previous model to see the effect of the new matrix properties on these behaviours.

Furthermore, the present model is described by a large number of variables that can potentially provide detailed information on the different components. However, the available experimental data are suited to validate only the fibrillar part of the tendon. Therefore, validating the model with experimental test about the matrix and fluid behaviour could help define those properties. In addition, the present model treats the components separately, while most probably their behaviours influence each other. Hence, further study could include the modelling of the interaction between the components.

Finally, including in the model the mechanics of gradual straightening of the fibers (i.e. fiber recruitment) as the mean to capture the non linear behaviour in 'toe' region could improve the overall representation of the tendon under cyclic loading.

A Determination of Jacobian for a single non-linear viscoelastic fiber

The implementation of the Jacobian in the ABAQUS subroutine UMAT requires the definition of the Cauchy stresses

$$\boldsymbol{\sigma}_f = \underbrace{\frac{1}{J}\frac{P_f^{t+\Delta t}}{\lambda}}_{\text{A}} \underbrace{\mathbf{F}\mathbf{e}_0\mathbf{e}_0^T\mathbf{F}^T}_{\mathbf{B}} \tag{56}$$

and the derivative with respect to the deformation tensor $\mathbf{F}$

$$\frac{\partial \boldsymbol{\sigma}_f}{\partial \mathbf{F}} = \mathbf{B}\frac{\partial A}{\partial \mathbf{F}} + A\frac{\partial \mathbf{B}}{\partial \mathbf{F}} \tag{57}$$

While the equation (56) can be implemented as shown, equation (57) can be expressed in known terms with further calculations. We repeat here useful relationships:

$$P_f^{t+\Delta t} = -\frac{b}{2} + \frac{1}{2}\sqrt{b^2 - 4c}\ , \tag{58}$$

$$\lambda = \frac{\| \mathbf{F} \cdot \mathbf{e}_{f,0} \|}{\| \mathbf{e}_{f,0} \|} = \frac{\| \mathbf{e}_f \|}{\| \mathbf{e}_{f,0} \|} \tag{59}$$

and

$$\epsilon_f^{n+1} = log(\lambda) \tag{60}$$

The term ϵ_f^{n+1} represents the fibril strain at the displacement increment $n+1$ (current strain), which corresponds to the time step $t + \Delta t$ in the numerical solution algorithm. The first derivative of the right side in equation (57) then equals

$$\frac{\partial A}{\partial \mathbf{F}} = \frac{1}{\lambda J}\frac{\partial P_f^{t+\Delta t}}{\partial \mathbf{F}} - \frac{P_f^{t+\Delta t}}{\lambda^2 J}\frac{\partial \lambda}{\partial \mathbf{F}} - \frac{P_f^{t+\Delta t}}{\lambda J^2}\frac{\partial J}{\partial \mathbf{F}} \tag{61}$$

where using the chain rule

$$\frac{\partial P_f^{t+\Delta t}}{\partial \mathbf{F}} = \frac{\partial P_f^{t+\Delta t}}{\partial \epsilon_f^{n+1}}\frac{\partial \epsilon_f^{n+1}}{\partial \lambda}\frac{\partial \lambda}{\partial \mathbf{F}} \tag{62}$$

The terms can now be expressed by known variables as

$$\frac{\partial P_f^{t+\Delta t}}{\partial \epsilon_f^{n+1}} = -\frac{1}{2}\frac{\partial b}{\partial \epsilon_f^{n+1}} + \frac{1}{2\sqrt{b^2 - 4c}}\left(b\frac{\partial b}{\partial \epsilon_f^{n+1}} - 2\frac{\partial c}{\partial \epsilon_f^{n+1}}\right)\ , \tag{63}$$

$$\frac{\partial \epsilon_f^{n+1}}{\partial \lambda} = \frac{1}{\lambda} \tag{64}$$

and

$$\frac{\partial \lambda}{\partial \mathbf{F}} = \frac{\partial}{\partial \mathbf{F}} \left(\sqrt{\mathbf{e}_0^T \mathbf{F}^T \mathbf{F} \mathbf{e}_0} \right) = \frac{1}{2} \frac{1}{\sqrt{\mathbf{e}_0^T \mathbf{F}^T \mathbf{F} \mathbf{e}^0}} 2 \mathbf{e}_0^T \mathbf{F} \mathbf{e}_0 = \frac{\mathbf{e}_0^T \mathbf{F} \mathbf{e}_0}{\lambda} \qquad (65)$$

Note that in equation (65) the denominator of λ was disregarded since the initial length of the fibril is assumed to equal 1. Then the last term in equation (57) equals

$$\frac{\partial \mathbf{B}}{\partial \mathbf{F}} = \frac{\partial}{\partial \mathbf{F}} \left(\mathbf{F} \mathbf{e}_0 \mathbf{e}_0^T \mathbf{F}^T \right) = 2 (\frac{\partial \mathbf{F}}{\partial \mathbf{F}} \mathbf{F} \mathbf{e}_0 \mathbf{e}_0^T) = 2 ({}^4\mathbf{I} \mathbf{F} \mathbf{e}_0 \mathbf{e}_0^T) \qquad (66)$$

Note also that $\mathbf{F}$ is assumed to be symmetric in all derivations.

References

[1] Wang J.H.-C., Mechanobiology of tendon, *Journal of Biomechanics*, 39 (2006) 1563-1582.

[2] Curwin S., Rehabilitation After Tendon Injuries, *Tendon injuries*, 24 (2005) 242-266.

[3] Nickisch F., Anatomy of the Achilles Tendon, *The Achilles Tendon: Treatment and Rehabilitation*, 1 (2009) 3-14.

[4] Möller A. et al., Increasing incidence of Achilles tendon rupture, *Acta Ortopedica*, 67 (1996) 479-481.

[5] James R. et al., Tendon: Biology, Biomechanics, Repair, Growth Factors, and Evolving Treatment Options, *The Journal of Hand Surgery*, 33 (2008) 102112.

[6] Sharma P. and Maffuli N., Tendon Injury and Tendinopathy: Healing and Repair, *The Jourmal of Bone & Joint Surgery*, 87 (2005) 187-202.

[7] Muller S. et al., Tendon healing: an overview of physyology, biology and pathology of tendon healing and systematic review of state of the art in tendon bioengineering, *Knee Surg. Sports Traumatol. Arthrosc*, 7 (2013) 680-88.

[8] Aygün H. et al., Tendon Healing and Repair: A review of Current Approaches, University of Kaftas.

[9] Lichtwark G.A. et al., In vivo mechanical properties of the human Achilles tendon during one-legged hopping, *Journal of Experimental Biology*, (2005)

[10] Suchack A. et al., The Influence of Early Weight-Bearing Compared with Non-Weight-Bearing After Surgical Repair of the Achilles Tendon, *The Jourmal of Bone & Joint Surgery*, 90 (2008) 1876-1883.

[11] Gustafsson A., A fiber-reinforced poroviscoelastic finite element model for the Achilles tendon, Department of Biomedical Engineering, Lund University (2014), Supervisor: Hanna Isaksson, Lund.

[12] Wilson W. et al., Stresses in the local collagen network of articular cartilage: a poroviscoelastic fibril-reinforced finite element study, *Journal of Biomechanics*, 37 (2004) 357-366.

[13] Julkunen P., Relationships between Structure, Composition and Function of Articular Cartilage, Doctoral Dissertation, Department of Physics, University of Kuopio (2008).

[14] Han S. et al., Change in ADC Caused by tensile loading of Rabbit Achilles Tendon: Evidence for Water Transport, *Journal of Magnetic Resonance*, 144 (2000) 217-227

[15] Atkinson T. et al., The tensile and stress relaxation responses of human patellar tendon varies with specimen cross-sectional area, *Journal of Biomechanics*, 32 (1999) 907914.

[16] Thornton G.M. et al., Altering ligament water content affects ligament pre-stress and creep behaviour, *Journal of Orthopaedic Research*, 19 (2001) 845-851

[17] Eliasson P., Fahlgren A., Pasternak B. and Aspenberg P., Unloaded rat Achilles tendons continue to grow, but lose viscoelasticity, *Journal of applied physiology (Bethesda, Md. : 1985)*, 103 (2007) 45963.

[18] Sharma P. and Maffuli N., Biology of tendon injury: healing, modeling and remodeling, *Journal of Muscoloskeletal Neural interaction*, 6 (2006) 181-190.

[19] Adeeb S. et al., Modelling the behaviour of Ligaments: A Technical Note, *Computer Methods in Biomechanics and Biomedical Engineering*, 7 (2004) 33-42.

[20] Maganaris C. and Narici M., Mechanical Properties of Tendons, *tendon Injuries*, 2 (2005) 14-21.

[21] Korhonen R. and Saarakkala S, Biomechiancs and Modeling of Skeletal Soft Tissues, *Theoretical Biomechanics*, (2011) 133-132.

[22] Fung Y.C., Biomechanics: mechanical properties of living tissues, Springer, Berlin Heidelberg New York, (1993).

[23] DeFrate L.E. and Li G., The prediction of stress-relaxation of ligaments and tendons using the quasi-linear viscoelastic model, *Biomechanics and Modeling in Mechanobiology*, 6 (2007) 245-251.

[24] Tang C.Y. et al., Parameter optimization for the visco-hyperelastic constitutive model of tendon using FEM, *Bio-Medical Mateials and Engineering*, 21 (2011) 9-24.

[25] Woo S. et al., Mathematical Modeling of Ligaments and Tendons, *Journal of Biomechanical Engineering*, 115 (1993) 468-473.

[26] PROVENZANO P. AND LAKES R., Nonlinear Ligament Viscoelasticity, *Annals of biomedical engineering*, 29 (2001) 908-914.

[27] LANIR Y., A Structural Theory fir the Homogeneous Biaxial stress-strain relationships in flat collagenous tissues, *Journal of Biomechanics*, 12 (1979) 423-436.

[28] LANIR Y., Constitutive equations for fibrous connective tissue, *Journal of Biomechanics*, 16 (1982) 1-12.

[29] LI L.P., BUSHMANN M.D. ET AL., A fibril reinforced nonhomogeneous poroelastic model for articular cartilage: inhomogeneous response in unconfined compression, *Journal of Biomechanics*, 33 (2000) 1533-1541.

[30] EINAT R. AND LANIR Y., Recruitment viscoelasticity of the tendon, *Journal of Biomechanical Engineering*, 131 (2009) 111008-1-8.

[31] CIARLETTA P., DARIO P. AND MICERA S., Pseudo model of the tendon hysteresis from adaptive recruitment of collagen type I fibrils, *biomaterials*, 29 (2008) 764-770.

[32] GUERIN H. AND ELLIOTT D., The Rome of Fiber-matrix interactions in a Nonlinear Fiber-Reinforced Strain Energy model of tendon, *Journal of Biomechanical Engineering*, 127 (2005), 345-350.

[33] WILSON W., An Explanation for the Onset of Mechanically Induced Cartilage Damage, Doctoral Dissertation, Technische Universiteit Eindhoven, Eindhoven, 2005.

[34] JULKUNEN P., WILSON W., JURVELIN J.S., RIEPPO J., QU C., LAMMI M.J. AND KORHONEN, R.K., Stress-relaxation of human patellar articular cartilage in unconfined compression: Prediction of mechanical response by tissue composition and structure, *Journal of Biomechanics*, 41 (2008) 19781986

[35] WILSON W. ET AL., Depth-dependent compressive equilibrium properties of articular cartilage explained by its composition, *Biomechaninc and Modeling in Mechanobiology*, 6 (2007) 43-53.

[36] YIN L. ET AL., A biphasic and transversly isotropic mechanical model for tendon: application to mouse tail fascicles in uniaxial tension, *Journal of Biomechnics*, 37 (2004) 907-16.

[37] WILSON W. ET AL., A composition-based cartilage model for the assessment of compositional changes during cartilage damage and adaptation, *OsteoArthritis and Cartilage*, 14 (2006) 554-560.

[38] Ottosen N. and Ristinmaa M., The Mechanics of Constitutive Modeling, Division of Solid Mechanics, Lund University, 2005.

[39] Itskov M., A generalized orthotropic hyperelastic material model with application to incompressible shells, *International Journal for Numerical Methods in Engineering*, 50 82001) 1777-99.

[40] Heuijerjans, A, Modeling of the Achilles tendon. Technical report, Solid Mechanics, Lund University (2012), Supervisor: Hanna Isaksson, Lund.

[41] Kuhl E. et al., Remodeling of biological tissue: Mechanically induced reorientation of a transversely isotropic chain network, *Journal of the Mechanics and Physics of Solids*, 53 (2005) 15521573.

[42] Shim V. et al., Subject-specific finite element analysis to characterize the influence of geometry and the material properties in Achilles tendon rupture, *Journal of Biomechanics*, 47 (2014) 3598-3604.

[43] Pioletti D.P. et al., Viscoelastic constitutive law in large deformations: application to human knee ligaments and tendons, *Journal of Biomechanics*, 31(1998) 753-757.

[44] Rigozzi S., Local strain measurement reveals a varied regional dependence of tensile tendon mechanics on glycosaminoglycan content, *Journal of Biomechanics*, 42 (2009) 15471552.

[45] Benjamin M. et al., The Anatomy of the Achilles Tendon, *The Achilles Tendon*, 3 (2007) 5-16.